

# Absolute and convective instability of cylindrical Couette flow with axial and radial flows

Denis Martinand,<sup>1</sup> Eric Serre,<sup>1</sup> and Richard M. Lueptow<sup>2</sup>

<sup>1</sup>*LM2P2 UMR 6181, CNRS, Universités d'Aix-Marseille, IMT, La Jeté-Technopôle de Château-Gombert, 38 rue Frédéric Joliot-Curie, 13451 Marseille Cedex 20, France*

<sup>2</sup>*Department of Mechanical Engineering, Northwestern University, Evanston, Illinois 60208, USA*

(Received 19 March 2009; accepted 8 September 2009; published online 7 October 2009)

Imposing axial flow in the annulus and/or radial flow through the cylindrical walls in a Taylor–Couette system alters the stability of the flow. Theoretical methods and numerical simulations were used to determine the impact of imposed axial and radial flows, homogeneous in the axial direction, on the first transition of Taylor–Couette flow in the framework of convective and absolute instabilities. At low axial Reynolds numbers the convective instability is axisymmetric, but convective helical modes with an increasing number of helices having a helicity opposite that of the base flow dominate as the axial flow increases. The number of helices and the critical Taylor number are affected only slightly by the radial flow. The flow becomes absolutely unstable at higher Taylor numbers. Absolutely unstable axisymmetric modes occur for inward radial flows, while helical absolute instability modes having a helicity identical to that of the base flow occur at high enough axial Reynolds numbers for outward radial flow. © 2009 American Institute of Physics.

[doi:[10.1063/1.3243976](https://doi.org/10.1063/1.3243976)]

## I. INTRODUCTION

In its simplest form, cylindrical Couette flow in an annulus between a rotating inner cylinder and a concentric, fixed outer cylinder becomes unstable at high enough rotational speed resulting in pairs of counter-rotating toroidal vortices stacked in the annulus. However, the stability of Taylor vortex flow is altered when an additional flow is superimposed. In particular, axial flow in the annulus or radial through-flow via porous walls of both cylinders can alter the conditions at which the supercritical transition occurs and can modify the supercritical vortex structure. The effect of axial flow, radial flow, and combined axial and radial flows on the absolute and convective stability of the flow and the nature of the vortex structure are examined in this paper. Pressure-driven axial flow with radial flow in an annulus between a rotating inner cylinder and a fixed outer cylinder has several important engineering applications including rotating filtration devices. In fact, rotating filtration, which is used for blood filtration<sup>1–3</sup> and has been proposed for filtering suspensions and water purification via reverse osmosis,<sup>4–10</sup> is one of the key applications that motivate this research, but the focus here is on the physics and underlying stability of the flow. It should then be emphasized that filtration devices and experimental setups involve the presence of porous cylinders to generate the radial flow, whereas the present analytical and numerical study focuses on the simpler situation of imposed nonzero wall-normal velocities on the cylinders.

Superimposing an axial flow in the annulus between a rotating inner cylinder and a fixed outer cylinder stabilizes the circular Couette flow so that the transition to supercritical Taylor vortex flow occurs at a higher Taylor number.<sup>11–24</sup> When the vortices appear, they translate in the same direc-

tion as the bulk axial flow in the annulus at 1–1.4 times the mean axial velocity.<sup>16,19–22,25–28</sup> The axial flow can also alter the character of the flow instability, resulting in helical vortices and wavy helical vortices.<sup>14–16,19,23,26–32</sup> It should be emphasized at this stage that Taylor–Couette flow with superimposed annular Poiseuille flow can also be seen as annular Poiseuille flow with superimposed azimuthal motion induced by the differential rotation of the cylinders, also known as spiral Poiseuille flow. Both centrifugal and shear instabilities can develop in such a system, depending on the relative importance of the azimuthal and axial motions.<sup>33–36</sup> Two features of the present study stem from the application of the system to filtration techniques. First, unlike most studies of spiral Poiseuille flow, this paper does not consider a rotating outer cylinder. Second, this paper focuses on centrifugal instabilities, i.e., those occurring for a limited axial mean velocity, the effect of which is therefore restricted to advecting the instabilities. Furthermore, owing to the supercritical nature of these centrifugal instabilities, the modal stability analysis encompasses most of the dynamics. Transient, nonmodal instabilities, pivotal in the case of shear instabilities,<sup>37</sup> are of limited interest here and are not addressed.

A net radial through-flow in the annulus between two differentially rotating porous cylinders also affects the absolute stability of the Taylor vortex flow. Linear stability indicates that radially inward flow and strong radially outward flow have a stabilizing effect, while weak radially outward flow destabilizes the system.<sup>22,32,38–42</sup> This result has been replicated computationally for imposed nonzero wall-normal velocities,<sup>43</sup> and the stabilizing effect also appears for radial inflow through a single inner porous cylinder rotating within a nonporous outer cylinder.<sup>31</sup> The latter is the situation that occurs in rotating filtration in which a suspension flows axi-

ally in the annulus while pure fluid is extracted through the inner porous cylinder.<sup>44</sup> Returning to the situation of interest here, i.e., nonvanishing wall-normal velocities on both cylinders associated with a radial inflow or outflow, the competition between the imposed radial velocity and the radial velocity related to the Taylor vortices may explain the effect of an imposed radial flow on the stability of the system.<sup>43</sup> In addition, not only does the radial flow alter the first transition from subcritical to supercritical flow, it also stabilizes the second transition from Taylor vortex flow to wavy vortex flow and directly affects the phase speed of the wavy vortices.<sup>43</sup>

The combined effects of axial and radial flow on the stability of Taylor vortex flow can also be studied using linear stability analysis following generally the same approach as that for axial or radial flow individually, although the imposition of both flows simultaneously complicates the analysis. The first attempt at the linear stability analysis for this case considered the narrow gap case for corotating porous cylinders with an axial flow, although the analysis suffered from a simplistic axial velocity profile and fixed values for the axial wave number and amplification factor.<sup>45</sup> More sophisticated analyses avoided these limitations and considered both axisymmetric and nonaxisymmetric perturbations at various radius ratios.<sup>22,32</sup>

Imposing an axial flow in a cylindrical Couette system of porous cylinders with radial flow naturally brings about the need to consider the convective and absolute instability limits. In fact, cylindrical Couette flow with an axial flow (but no radial flow) has been used as a model for introducing and studying the distinction between absolutely unstable flow and convectively unstable flow for low axial Reynolds number and Taylor numbers very near the transition to vortical flow. Depending on the properties of the impulse response, the behavior of the flow can be classified as unconditionally stable, convectively unstable, and absolutely unstable as follows (see Refs. 46 and 47 for a review on the hydrodynamics of convective and absolute instabilities).

Unconditionally stable flow is characterized by any perturbation to the flow decaying, so vortices do not form. Convectively unstable flow is distinguished by the situation in which a localized perturbation cannot propagate upstream but will grow as it is advected downstream until it is carried out of the system. Without a permanent source of perturbations, the system returns to the basic stable state everywhere. Convectively unstable flow is evident experimentally in two forms.<sup>20,48,49</sup> In the first form, a localized perturbation is introduced experimentally by rotating both cylinders back and forth once through a small angle or by moving the inlet boundary forward and back one time. The resulting pulse consists of two or three vortex pairs near the upstream end of the test cell where no vortices are otherwise present. The vortex pairs propagate axially with the axial flow while growing in amplitude and number as they proceed downstream. In the second form, the perturbation is the inherent noise in the system resulting in the appearance of axially propagating vortices. In both situations, convectively unstable flow occurs at increased driving conditions (higher Taylor number) and smaller axial flow conditions (lower

axial Reynolds number) than the unconditionally stable flow regime. Absolutely unstable flow is characterized by localized perturbations that grow and spread both upstream and downstream. This flow regime occurs at larger driving conditions and smaller axial flow conditions than convectively unstable flow. The flow itself appears similar to that for noise-sustained propagating vortices in the convectively unstable regime, but there are several differences.<sup>20,48</sup> First, the boundary between the nonvortical flow entering the annulus and the propagating vortices is stationary for absolutely unstable flow, but is time dependent for convectively unstable flow. Nevertheless, it should be emphasized that this amounts to the nonlinearity or the nonhomogeneity of the flow. Second, the distance from the axial flow inlet to the boundary between nonvortical and vortical flows scales differently in the two flow regimes. Finally and more importantly, the power spectrum of the propagating vortex velocity is noisier for the convectively unstable regime than for the absolutely unstable regime. This last property underlines the different nature of convectively and absolutely unstable flows: while the former behaves as a noise amplifier acting on all the wave numbers and frequencies present in the forcing, the latter behaves as a resonator prone to select specific wave number and frequency.

The impact of radial flow on the convective and absolute instability for axial flow superimposed on Taylor–Couette flow has not been studied due to the inherent difficulties in building an experimental setup with both inner and outer porous cylinders and the challenges in computational simulations of the flow. The case of a single rotating inner porous cylinder, however, has been studied in some detail experimentally.<sup>31</sup> In this situation, the source for the fluid that exits radially at the porous inner cylinder is the axial flow. Consequently, the axial flow decreases along the length of the annulus as fluid is removed. Helical vortices appear at high Taylor numbers, but they appear in packets of five or six helical vortex pairs with alternating signs for the helix angles so that helices of both signs appear in different portions of the annulus simultaneously. Since fluid is being lost through the porous inner cylinder as the vortices translate with the axial flow, the wavelength of a vortex decreases as it travels axially in the annulus. The stability of the flow with an inner porous cylinder and an outer nonporous cylinder with an axial flow has not been studied analytically because of the difficulty in obtaining an analytic solution for the stable flow. Recent progress toward a solution based on a generalized similarity formulation provided an initial step toward resolving this problem, but determining the stability with respect to three-dimensional perturbations is still quite difficult.<sup>50</sup>

In this paper we take a two-pronged approach to studying the stability of Taylor–Couette flow with an imposed radial through-flow (two porous cylinders) and an imposed axial flow. First, we consider the convective and absolute instabilities of the flow using theoretical methods. Second, we use direct numerical simulations to confirm the theoretical results and visualize the vortex structure.

The material is organized as follows. Section II presents the geometry and the analytical solutions for the base flow in a Taylor–Couette system with superimposed homogeneous

axial and radial flows. Section III describes the theoretical and numerical methods used for the convective/absolute stability analysis and assesses their reliability and accuracy. The theoretical and numerical results pertaining to this analysis are discussed in Sec. IV. Finally, concluding remarks and possible extensions of this work are addressed in Sec. V.

## II. GEOMETRY AND STEADY FLOW

An annular cavity between two concentric cylinders of inner and outer radii  $R_{in}$  and  $R_{out}$  is considered, with the inner cylinder rotating at angular speed  $\Omega$  and the outer cylinder stationary. Departing from the usual Taylor–Couette setup, an imposed pressure gradient along the length of the annulus drives an axial flow, and a uniform wall-normal radial velocity is prescribed at the inner and outer cylinders as  $U_{in}$  and  $U_{out}$ , respectively. Using cylindrical coordinates  $(r, \theta, z)$ , the radial, azimuthal, and axial components of the velocity field  $(u, v, w)$  and the pressure field  $p$  satisfy the continuity and incompressible three-dimensional Navier–Stokes equations. Apart from the prescribed wall-normal velocity, surfaces are no-slip, imposing zero relative tangential velocities on the cylinders.

A laminar steady flow  $(u_b(r), v_b(r), w_b(r), p_b(r))$ , which will act as the base flow in the analyses to come, can be determined analytically. Nondimensional parameters of the system are then the following:

- the radius ratio  $\eta = R_{in}/R_{out}$ ;
- for the computations in a finite length cavity, the aspect ratio  $\Gamma = h/d$ , where  $h$  is the distance between the ends of the annulus and  $d = (R_{out} - R_{in})$  is the gap (for the theoretical analysis the cylinders are infinitely long);
- the Taylor number  $Ta = R_{in}\Omega d/\nu$ , where  $\nu$  is the kinematic viscosity (also called a rotating or inner Reynolds number in this form, it is referred to as the Taylor number to avoid confusion with the other two Reynolds numbers in the problem; unlike some existing definitions of the Taylor number proportional to  $\Omega^2$ , the present one is proportional to the azimuthal velocity of the inner cylinder);
- the radial Reynolds number  $\alpha = U_{in}R_{in}/\nu$  ( $=U_{out}R_{out}/\nu$ , owing to continuity); and
- the axial Reynolds number  $\beta = \bar{w}d/\nu$  where  $\bar{w} = (R_{out}^2 - R_{in}^2)^{-1} \int_{R_{in}}^{R_{out}} w_b(r) 2r dr$ .

Following Ref. 32, the incompressible Navier–Stokes and continuity equations are made nondimensional by introducing the following scales:  $d$  for the lengths,  $\tau = d^2/\nu$  for the times,  $v = \Omega d$  for the velocities, and  $\pi = \rho\nu\Omega$  for the pressure. Unless stated, the quantities hereinafter are nondimensional. Expressions for the base flow including the specific cases  $\alpha = -2, 0$ , and  $2$  can be found in the Appendix. An example of such a base flow is depicted in Fig. 1 using an unusually low value of  $Ta$  to magnify the radial and axial components of the velocity.

The radius ratio has been kept constant at  $\eta = 0.85$  to

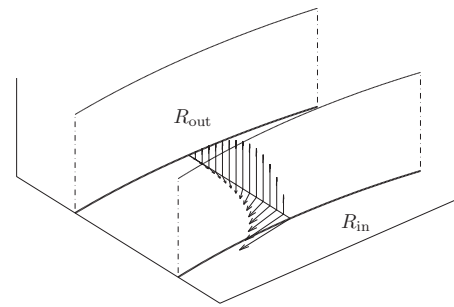


FIG. 1. The base flow for  $\eta = 0.85$ ,  $\alpha = -20$ ,  $\beta = 20$ , and  $Ta = 20$  decomposed into the horizontal component  $(u_b, v_b, 0)$  and the vertical one  $(0, 0, w_b)$ .

match a broad range of experiments and simulations for this and similar radius ratios. Consistent with rotating filtration devices, the outer cylinder has been kept fixed. Although the analysis conducted here can relax these two constraints, it would, of course, dramatically increase the scope of the parametric study. This study therefore mostly focuses on the influence of the radial and axial flows. Radial Reynolds numbers in the range of  $-20 \leq \alpha \leq 20$  and axial Reynolds numbers in the range of  $0 \leq \beta \leq 50$  have been considered again to allow comparison with previous results and provide information in the range that is representative of rotating filtration devices ( $-10 \leq \alpha \leq -0.1$  and  $0 \leq \beta \leq 50$ ).<sup>22</sup>

## III. METHODS

### A. Convective and absolute stability analysis

The analytical approach focuses on determining the critical thresholds between unconditional stability and convective instability on the one hand and convective instability and absolute instability on the other hand as well as the characteristics of the associated critical modes. These stability analyses amount to the impulse response of the linear stability operator derived from the continuity and Navier–Stokes equations. Strictly speaking, their scope is restricted to configurations that are homogeneous in the axial direction. As usual, the velocity and pressure fields are decomposed into the steady laminar base flow  $(u_b, v_b, w_b, p_b)$  of Sec. II and temporally evolving perturbations  $(u_p, v_p, w_p, p_p)$ . The continuity and Navier–Stokes equations linearized about the base flow yield a system of partial differential equations satisfied by  $(u_p, v_p, w_p, p_p)$ . Seeking these perturbations in the form  $(u_p, v_p, w_p, p_p) = (u(r), v(r), w(r), p(r)) \exp(-i\omega t + ikz + in\phi)$  recasts these partial differential equations into the following eigenvalue problem:

$$\omega \mathbf{X} = \mathcal{A} \mathbf{X}, \quad (1)$$

together with vanishing boundary conditions for the velocity on the inner and outer radii. The eigenvectors of Eq. (1) are the radial dependences  $\mathbf{X}(r) = (u(r), v(r), w(r), p(r))^T$ , associated with their respective eigenvalues for the complex frequency  $\omega$ . The differential operator  $\mathcal{A}$  is



TABLE I. Comparison between results from the literature and present for the critical Taylor numbers  $Ta_{crit}^{conv}$  and  $Ta_{crit}^{abs}$ .

Ref.	$\eta$	$\alpha$	$\beta$	$n$	$Ta_{crit}^{conv}$		$Ta_{crit}^{abs}$	
					Literature	Present	Literature	Present
21	0.8	0	0	0	94.73	94.73		
			5		95.64	95.64	111.80	111.44
			10		98.33	98.33	150.36	150.41
			15		102.72	102.72	194.62	201.69
			20		108.68	108.68	236.77	304.59
27	0.95	0	20	1	211.69	211.68		
19	0.5	0	30	1	86.62	86.62		
35	0.77	0	49	3	148.44	148.45		
			63.5	7	165.15	165.16		
			166	17	193.34	193.32		
			403.5	20	196.02	196.03		
22	0.85	-15	0	0	155.79	155.79		
		0			108.31	108.31		
		15			108.57	108.57		

convective ( $Ta_{crit}^{conv}$ ) and absolute ( $Ta_{crit}^{abs}$ ) instabilities in the case of Taylor–Couette flow with a superposed axial flow but devoid of any radial flow ( $\alpha=0$ ) can be compared to previous results from the existing literature<sup>21</sup> for  $\eta=0.8$ ,  $n=0$ , and various values of  $\beta$ . It can be observed in Table I that, whereas the agreement is excellent as far as  $Ta_{crit}^{conv}$  is concerned, it deteriorates for  $Ta_{crit}^{abs}$  as  $\beta$  increases. It should be noted that in Ref. 21, the derivatives  $\partial_k \omega$ ,  $\partial_k^2 \omega$ , and  $\partial_{Ta} \omega$  were evaluated from the dispersion relation itself, i.e., from  $\omega$  computed from various values of  $k$  and  $Ta$ , whereas our method allows an exact computation of these derivatives, which should be more accurate. Furthermore, the  $Ta_{crit}$  in Ref. 21 are given in the form of fits as functions of  $\beta$  within the range  $0 \leq \beta \leq 20$ , and we compare our direct calculation of  $Ta_{crit}$  to the values extracted from these fits. Further validations for  $\alpha=0$  but  $n \neq 0$  were obtained by comparison with Refs. 19, 27, and 35 and showed excellent agreement (see Table I). The case  $\alpha=0$  requires a specific treatment to compute the operator  $\mathcal{A}$ . So the present computations have been compared to previous results<sup>22</sup> for various values of  $\alpha$  with  $\beta=0$  and  $n=0$ , i.e., in the case of Taylor–Couette flow with superposed radial flow but devoid of axial flow. The agreement is again excellent (see Table I).

## B. Computations

For the numerical simulations of the incompressible Navier–Stokes equations, we employed a pseudospectral Chebyshev-collocation Fourier–Galerkin method that is identical to that used in our previous work.<sup>43,51–55</sup> Time integration was accomplished with a second-order backward implicit Euler scheme for the linear terms and a second-order explicit Adams–Bashforth scheme for the nonlinear terms.<sup>56</sup> An improved projection algorithm was employed for velocity–pressure coupling.<sup>57</sup>

The height of the cavity was set to  $h=50$ . The mesh

grid was defined by the Gauss–Lobatto–Chebyshev collocation points with  $n_r=21$  and  $n_z=301$  points in the radial and axial directions, respectively. In the azimuthal direction,  $n_\phi=12$  equally spaced mesh points were used. The associated time step was  $\delta t=4 \times 10^{-3} Ta^{-1} \eta / (\eta - 1)$ . Previous validation<sup>43,52,53</sup> has shown the method to be in good agreement with theory<sup>21,22,42</sup> and measurements.<sup>58</sup>

The boundary conditions at the ends of the annulus were complicated by the axial flow entering and exiting the flow domain. The velocity profile expressed in the Appendix, encompassing the azimuthal, axial, and radial laminar flows, was imposed at the inlet (only cases with  $\beta \neq 0$  have been addressed numerically). A buffer region of length  $0.1h$  extending upstream from the exit of the domain was used to exponentially damp the perturbation and recover the analytic base flow at the outlet.

The initial conditions were obtained by adding to the laminar flow given in the Appendix a disturbance at the inlet on the axial component of the velocity and consisting of a sum of sine functions of azimuthal periodicity  $2\pi/k$  with  $k$  ranging from 1 to 4. The amplitude of this disturbance was set to 0.1% of the laminar flow amplitude.

To confirm consistency between the numerical simulations and the analytic, the value for  $Ta_{crit}^{conv}$  obtained by numerical simulation was compared to the analytic value for  $\alpha=1$  and  $\beta=2$ . Numerically, this was done by determining  $Ta_{crit}^{conv}$  from the growth rates  $\text{Im}(\omega)$  for the axisymmetric ( $n=0$ ) component of the velocity field of the perturbation for three  $Ta$  near the transition. The overall rms amplitude of the velocity fluctuations ( $u_0, v_0, w_0$ ) for the  $n=0$  mode (the most unstable one), after filtering the other modes, is plotted as a function of time in Fig. 2(a). The growth rates extracted from the linear portion of the curves are plotted in Fig. 2(b). The value for  $Ta_{crit}^{conv}$  from the simulation is 107.71, very similar to the analytical prediction  $Ta_{crit}^{conv}=107.25$ .

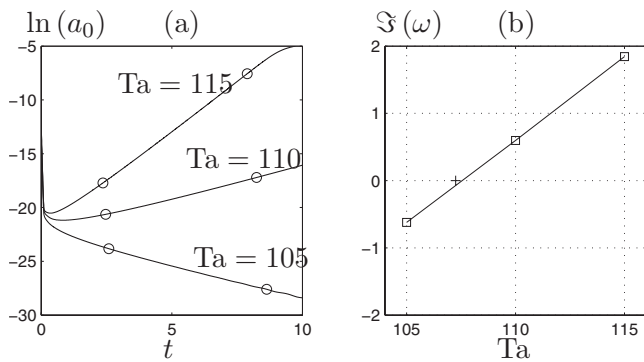


FIG. 2. (a) Numerically obtained natural logarithm of the rms amplitude  $a_0 = \sqrt{u_0^2 + v_0^2 + w_0^2}$  of the  $n=0$  mode as a function of time for  $Ta=105, 110,$  and  $115$  with  $\alpha=1$  and  $\beta=2$ . The growth rates  $\text{Im}(\omega)$  associated with the linear dynamics of the system are computed by linear fits between the  $\circ$ 's in (a). (b) The value for  $Ta_{\text{crit}}^{\text{conv}}$  obtained using the numerical growth rates matches the analytical prediction (+).

IV. RESULTS

The instabilities in a Taylor–Couette flow with superimposed axial and radial flows, axisymmetric and helical modes have been evaluated with  $n$  ranging from  $-30$  to  $30$  for both convective and absolute instabilities. Analytically obtained critical conditions in terms of critical Taylor numbers above which an unstable mode grows are presented in Fig. 3 for the convective instability. On a broad scale, the axial flow ( $\beta > 0$ ) stabilizes the Taylor–Couette system, whereas a small amount of positive radial flow ( $0 < \alpha < 15$ ) slightly destabilizes the system with respect to convective instabilities, consistent with previous theoretical and numerical results limited to  $n=0$ .<sup>22,31,43</sup>

At the lowest axial Reynolds numbers, the vortices are toroidal ( $n=0$ ). Figure 3 sheds light on the fact that helical modes become the most unstable convective instabilities as  $\beta$  increases further, whereas  $\alpha$  only slightly affects this selection. Helical vortices are always “left handed” or “inverse threaded,” i.e., with positive  $k$  and  $n$ , consistent with previous results.<sup>16,19,26,59</sup> Thus, the helicity of the vortex structure is opposite the helicity of the base flow. For  $\alpha=0$ , the marginal mode becomes a single helix ( $n=1$ ) at  $\beta=14$  and leading to  $Ta_{\text{crit}}^{\text{conv}}=116.3$ , compared to  $Ta_{\text{crit}}^{\text{conv}}=108.3$  for  $\beta=0$  ( $n=0$ ). This result is comparable to experimental data, which indicates this transition is between  $\beta=7$  and  $\beta=9$  with  $Ta_{\text{crit}}^{\text{conv}} \sim 110\text{--}120$  (see Fig. 4 in Ref. 26 and Fig. 2 in Ref. 28). The same experiments also locate the critical conditions for  $\beta=25$  at  $Ta_{\text{crit}}^{\text{conv}} \sim 138\text{--}146$ , favorably comparing with the present predicted value  $Ta_{\text{crit}}^{\text{conv}}=131.8$ . Increasing the axial Reynolds number to  $\beta=34$  with  $\alpha=0$ , the marginal mode becomes a double helix ( $n=2$ ). This transition was not noted in the only experiments with high values of  $\beta$ , but this may be accounted for by the experiments only extending to  $\beta=37$  (a single data point). Furthermore, as depicted in Fig. 4, marginal Taylor numbers  $Ta_n^{\text{conv}}$ , i.e., Taylor numbers yielding a zero growth rate at a fixed azimuthal wave number, in the vicinity of the most unstable azimuthal wave number remain fairly close to one another, suggesting that more than one azimuthal wave numbers may be unstable in an experiment. At still higher axial Reynolds number, the mar-

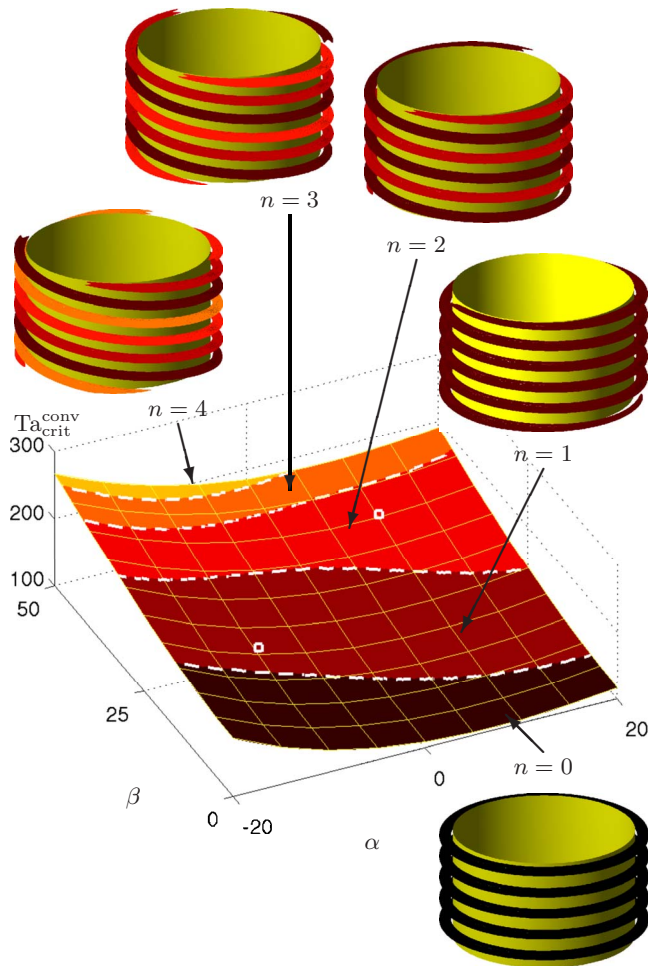


FIG. 3. (Color online) Critical Taylor number for the most unstable convective mode as a function of  $\alpha$  and  $\beta$ . Increasingly lighter shades represent  $n=0, 1, 2, 3,$  and  $4$ . The white dots locate the numerical simulations of Fig. 6 ( $\alpha=-10, \beta=20,$  and  $Ta=160$ ) and Fig. 8 ( $\alpha=10, \beta=40,$  and  $Ta=160$ ) in this parameter space. The insets sketch the toroidal mode ( $n=0$ ) and the single, double, triple, and quadruple helices ( $n=1, 2, 3,$  and  $4$ , respectively). These sketches do not account for the spatial modulation of the amplitude of the modes along the  $z$ -axis.

ginal mode is a triple helix ( $n=3$ ) at  $\beta=44$  and a quadruple helix at  $\beta=49$ . The destabilization of the flow by modes with increasingly large positive azimuthal wave numbers might be akin to the instability of an inviscid vortex in unbounded domains.<sup>60</sup> Without radial flow, such an instability occurs under the sufficient condition

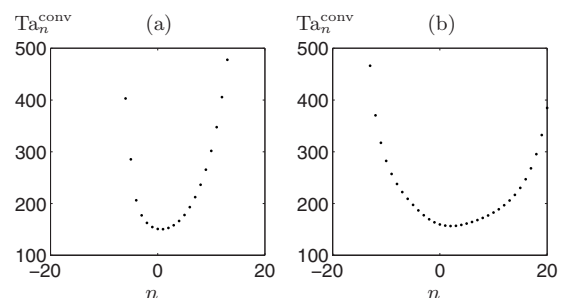


FIG. 4. Marginal Taylor numbers  $Ta_n^{\text{conv}}$  as functions of the azimuthal wave number  $n$  obtained at (a)  $\alpha=-10, \beta=20$  and (b)  $\alpha=10, \beta=40$ , corresponding to the white dots in Fig. 3.

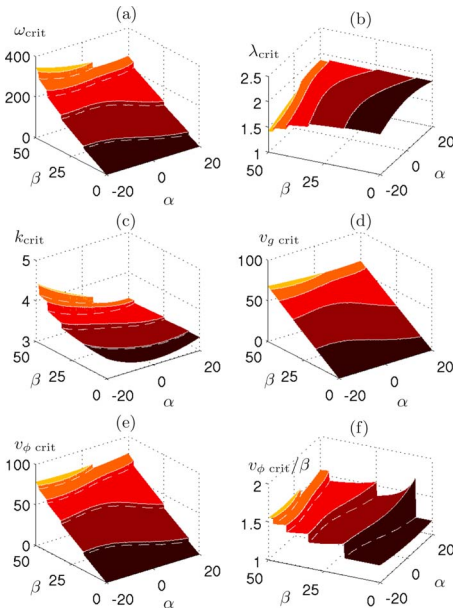


FIG. 5. (Color online) Critical quantities for the most unstable convective mode. (a) Temporal frequency  $\omega_{\text{crit}}$ ; (b) wavelength  $\lambda_{\text{crit}}=2\pi(k_{\text{crit}}^2+n^2/\bar{r}^2)^{-1/2}$  where  $\bar{r}=(1+\eta)/2(1-\eta)$  is the mean radius and  $k_{\text{crit}}$  is the axial wave number, also depicted in (c); (d) group velocity  $v_{g \text{ crit}}=(\partial\omega/\partial k)_{\text{crit}}$ ; (e) phase speed  $v_{\phi \text{ crit}}=\omega_{\text{crit}}/k_{\text{crit}}$ ; and (f) phase speed to axial Reynolds number ratio. These quantities are evaluated at the critical threshold for the most unstable convective mode in Fig. 3. Increasingly lighter shades represent  $n=0, 1, 2, 3,$  and  $4,$  respectively. The solid and dashed white lines highlight the upper and lower limits, respectively, of the jumps of the plotted quantities as  $n$  changes.

$$v_b \frac{dv_b/r}{dr} \left[ \frac{dv_b/r}{dr} \frac{drv_b}{dr} + \left( \frac{dw_b}{dr} \right)^2 \right] < 0. \quad (10)$$

Nonetheless, this condition being satisfied in the present flow for all values of  $\beta$  and  $Ta$ , it does not allow us to discriminate the effect of the viscosity from the relevance of such instabilities to explain the existence of a critical Taylor number. For  $\alpha \neq 0$ , helical modes are still obtained analytically to be the most unstable. The only experiments for  $\alpha \neq 0$  are for a porous inner cylinder and a nonporous outer cylinder.<sup>31</sup> In this case, the imposition of a radial flow causes helical vortices to be replaced by toroidal vortices. Of course, analytically and numerically, the radial flow is imposed at both cylinders and the axial and radial flows are invariant along the  $z$ -axis. Experimentally, the radial flow was only through the inner porous and the radial and axial flows both varied substantially in the axial direction.

The analytical stability analysis also yields several quantities characterizing the marginal mode at critical conditions, including the temporal frequency  $\omega_{\text{crit}}$ , the wave number  $k_{\text{crit}}$ , and wavelength  $\lambda=2\pi(k_{\text{crit}}^2+n^2/\bar{r}^2)^{-1/2}$ , where  $\bar{r}=(1+\eta)/2(1-\eta)$  is the mean radius, the group velocity  $v_{g \text{ crit}}=(\partial_k\omega)_{\text{crit}}$ , the phase speed  $v_{\phi}=\omega_{\text{crit}}/k_{\text{crit}}$ , and the phase velocity compared to the bulk axial velocity  $v_{\phi}/\beta$ . The dependencies of these quantities on  $\alpha$  and  $\beta$  are shown in Fig. 5. The temporal frequency  $\omega_{\text{crit}}$  and the wave number  $k_{\text{crit}}$ , shown in Figs. 5(a) and 5(c), both increase smoothly with  $\beta$  for a given value of  $n$  and increase sharply as  $n$  changes. Consistent with analytic results over much more limited

ranges of  $\alpha$  and  $\beta$ ,<sup>22,32,42</sup> the wave number is a minimum at small positive values of  $\alpha$ . It increases slightly with large positive values of  $\alpha$  and increases substantially for large negative values of  $\alpha$ , particularly at high  $\beta$ . The wavelength, shown in Fig. 5(b), is maximum for small  $\beta$  at about  $2.0d$  and decreases with increasing  $\beta$ , particularly for large negative  $\alpha$ . There are little experimental data for the wavelength near critical conditions, except for  $\eta=0.83, \beta=2.3, \alpha=0, Ta=108$  (corresponding to  $n=0$ ) for which  $\lambda/d=1.85$  and  $\beta=14, \alpha=0, Ta=122$  (corresponding to  $n=1$ ) in which case  $\lambda/d=1.9$ .<sup>28</sup> These are very near the analytic values of  $\lambda/d=1.95$  obtained at  $Ta_{\text{crit}}^{\text{conv}}=102.33$  and  $\lambda/d=1.87$  obtained at  $Ta_{\text{crit}}^{\text{conv}}=109.71$ , respectively. Further from critical conditions, for  $\eta=0.848, \beta=7, \alpha=0,$  and  $Ta=120$  (corresponding to  $n=0$ ),  $\lambda/d=2.1$ , and for  $\beta=10, \alpha=0,$  and  $Ta=130$  (corresponding to  $n=1$ ),  $\lambda/d=2.0$ .<sup>26</sup> These remain relatively close to the analytic values of  $\lambda/d=1.92$  obtained at  $Ta_{\text{crit}}^{\text{conv}}=109.65$  and  $\lambda/d=1.85$  obtained at  $Ta_{\text{crit}}^{\text{conv}}=112.03$ , respectively. Of course, increasing the departure from critical conditions reduces the ability of the linear analysis to match experiments. The phase speed  $v_{\phi \text{ crit}}=\omega_{\text{crit}}/k_{\text{crit}}$ , which is the velocity at which the vortices translate, increases with  $\beta$ , with jumps as  $n$  increases, but is relatively independent of  $\alpha$ , as shown in Fig. 5(e). For convective instabilities, the wave vector is real and, therefore, at the critical threshold, the group velocity  $v_{g \text{ crit}}=(\partial\omega/\partial k)_{\text{crit}}$ , namely, the velocity at which the wave packet travels downstream, is also real. The group velocity remains continuous as  $\beta$  and, consequently,  $n$  increase and is relatively independent of  $\alpha$ , as shown in Fig. 5(d). The phase velocity is slightly higher than the group velocity. For comparison with experiments, it is helpful to consider the ratio of the phase velocity to the average axial velocity of the base flow in dimensionless form  $v_{\phi}/\beta$ , shown in Fig. 5(f). At low  $\beta$ , the ratio is about 1.2, consistent with experimental values for the vortex translation speed  $w_{\text{vortex}}/\bar{w}$ .<sup>28</sup> As  $\beta$  increases, the velocity of the vortices decreases for constant  $n$ , but increases sharply with transitions in  $n$ . These results are generally consistent with experimental results, although the experiments show a wide range of vortex velocities ( $0.7 \leq w_{\text{vortex}}/\bar{w} \leq 2.2$ ). Of course, much of the experimental data are not at transition conditions, so they are not directly comparable with the analytic results.

The convection of a single-helix ( $n=1$ ) wave packet based on numerical simulations is shown in Fig. 6 for the condition indicated by one of the dots in Fig. 3 (at  $\alpha=-10, \beta=20,$  and  $Ta=160$  to be compared to  $Ta_{\text{crit}}^{\text{conv}}=150.25$ ), confirming the analytic prediction for the selected pattern. Interestingly, the wave packet begins with a right-handed sense ( $n=-1$ ). As it progresses, the sense of the helix becomes left handed ( $n=1$ ) for the leading portion and right handed ( $n=-1$ ) for the trailing portion with a discontinuity in about the middle of the wave packet. This is not surprising given that the  $n=-1$  mode is nearly as unstable as the  $n=1$  mode. The spatiotemporal propagation of the numerically obtained wave packet is shown in Fig. 7. The wave packet initially grows in both the number of waves and amplitude as it propagates axially, but then diminishes near the downstream end due to the boundary condition at the exit of the annulus.

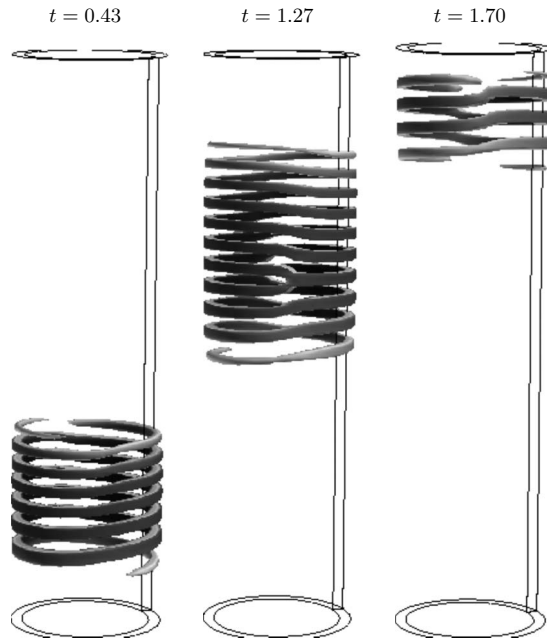


FIG. 6. Numerically obtained temporal evolution of the wave packet for  $Ta=160$ ,  $\alpha=-10$ ,  $\beta=20$ , and  $\Gamma=50$ , exhibiting a convective mode with both  $n=1$  and  $n=-1$ . Surfaces are fluctuations of axial velocity at slightly different levels.

The analytic group velocity matches the velocity of the wave packet in the simulations.

The propagation of a double helix ( $n=2$ ) wave packet based on numerical simulations is shown in Fig. 8 for the condition indicated by the other dot in Fig. 3 (at  $\alpha=10$ ,  $\beta=40$ , and  $Ta=160$  to be compared to  $Ta_{crit}^{conv}=156.41$ ), also in agreement with the analytic prediction for  $n$ . In this case, the sense of wave packet is always left handed ( $n$  positive). The match between the analytic group velocity and the numerically obtained propagation is not quite as good in this case, with the analytic value slightly higher, as shown in Fig. 9. Again the amplitude and number of waves in the wave packet grow as it propagates.

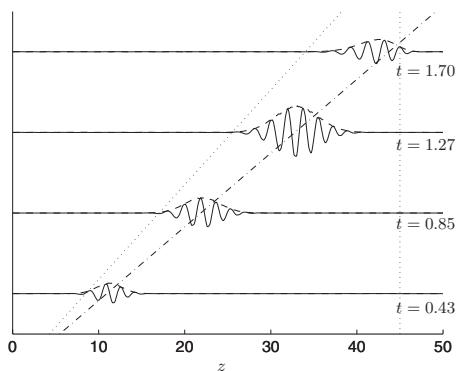


FIG. 7. Numerically obtained spatiotemporal evolution of the wave packet for  $Ta=160$ ,  $\alpha=-10$ , and  $\beta=20$  in the form of the axial velocity (—) and its spatial Hilbert transform (---), compared to the positions of the maximum of the wave packet inferred from the analytical group velocity  $v_g=25.72$  (- · -), and of the point originally at  $z=0$  and traveling at the mean nondimensional axial velocity  $\beta=20$  (···). The buffer region used in the numerical simulation extends between  $z=45$  (···) and the outlet at  $z=50$ .

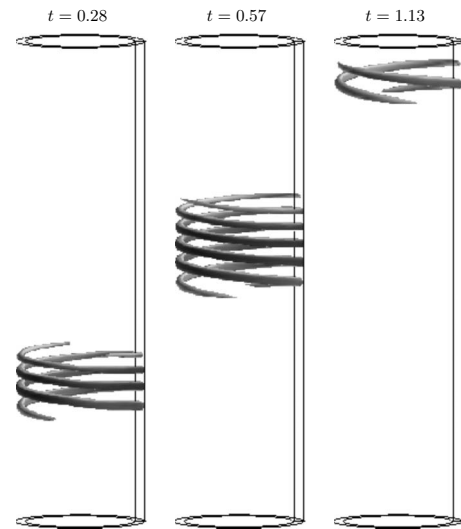


FIG. 8. Numerically obtained temporal evolution of the wave packet for  $Ta=160$ ,  $\alpha=10$ ,  $\beta=40$ , and  $\Gamma=50$ , exhibiting a convective mode with  $n=2$ . Surfaces are fluctuations of axial velocity at slightly different levels at  $t=0.28$  and  $t=0.57$  while the surface at  $t=1.13$  is plotted at a significantly lower level.

The flow becomes absolutely unstable at much higher Taylor numbers, as shown in Fig. 10. At higher values of  $\beta$  and positive values of  $\alpha$  the nonaxisymmetric modes become the most absolutely unstable ones. However, unlike convective instabilities, these single-helix modes are right handed with positive  $k$  and  $n=-1$ . For negative values of  $\alpha$  the axisymmetric modes remain the most unstable even for large  $\beta$ . The radial flow also has a greater influence on the critical Taylor number for negative values of  $\alpha$  than for positive values.

The critical frequency increases with  $\beta$ , with the greatest value for large negative  $\alpha$ , as shown in Fig. 11(a). The critical frequency is also substantially lower than that for the convectively unstable situation and increasing the algebraic

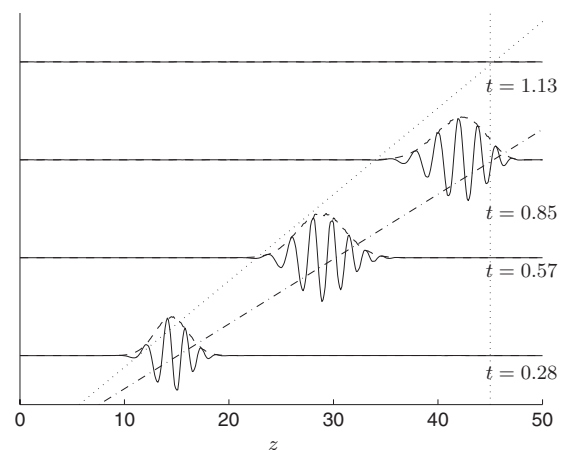


FIG. 9. Numerically obtained spatiotemporal evolution of the wave packet for  $Ta=160$ ,  $\alpha=10$ , and  $\beta=40$  in the form of the axial velocity (—) and its spatial Hilbert transform (---), compared to the expected position of the maximum of the wave packet inferred from the analytical group velocity (- · -), and of the point originally at  $z=0$  and traveling at the mean nondimensional axial velocity  $\beta=40$  (···). The buffer region is between  $z=45$  (···) and  $z=50$ .

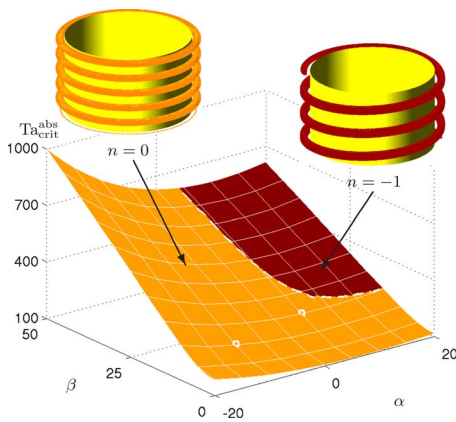


FIG. 10. (Color online) Critical Taylor number for the most unstable absolute mode as a function of  $\alpha$  and  $\beta$ . Increasingly lighter shades stand for  $n=-1$  and 0. The insets sketch the toroidal mode ( $n=0$ ) and the right-handed single-helix  $n=-1$  mode. These sketches do not account for the imaginary part of the axial wave number. The white dots locate the numerical simulations of Fig. 12 ( $\alpha=-10$ ,  $\beta=10$ , and  $Ta=215$ ) and Fig. 15 ( $\alpha=5$ ,  $\beta=15$ , and  $Ta=220$ ) in this parameter space.

value of  $n$  increases the frequency. Unlike the convective instabilities, the wavelength of the absolute modes strongly increases with  $\beta$  and substantially departs from the ubiquitous value of 2, as shown in Fig. 11(b). This is due to the sharp decrease in  $\text{Re}(k_{\text{crit}})$ , shown in Fig. 11(c). Interestingly, elongated rolls with wavelengths of 3.0–3.4 have been observed experimentally for  $\alpha=0$ ,  $\beta=3-10$ , and

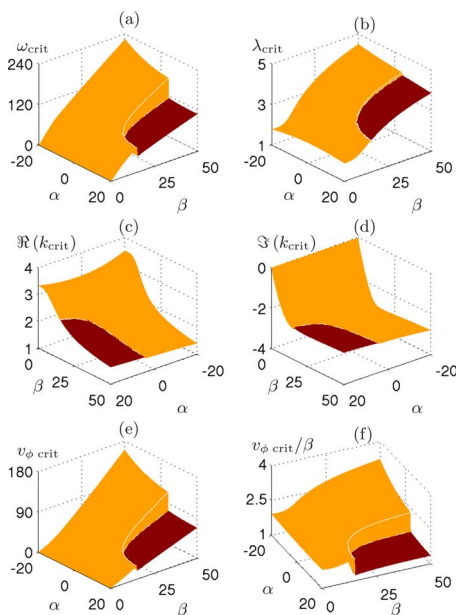


FIG. 11. (Color online) Critical quantities for the most unstable absolute mode. (a) Temporal frequency  $\omega_{\text{crit}}$ ; (b) wavelength  $\lambda_{\text{crit}}=2\pi[\text{Re}(k_{\text{crit}})^2+n^2/\tau^2]^{-1/2}$ ; (c) real part of the axial wave number  $\text{Re}(k_{\text{crit}})$ ; (d) imaginary part of the axial wave number  $\text{Im}(k_{\text{crit}})$ ; (e) phase speed  $v_{\phi \text{ crit}}=\omega_{\text{crit}}/\text{Re}(k_{\text{crit}})$ ; and (f) phase speed to axial Reynolds number ratio. These quantities are evaluated at the critical threshold for the most unstable absolute mode in Fig. 10. Note that the specific orientations of the axes vary in the different figures to conveniently display the surfaces. Increasingly lighter shades represent  $n=-1$  and 0, respectively. The solid and dashed white lines highlight the upper and lower limits, respectively, of the jumps of the plotted quantities as  $n$  changes.

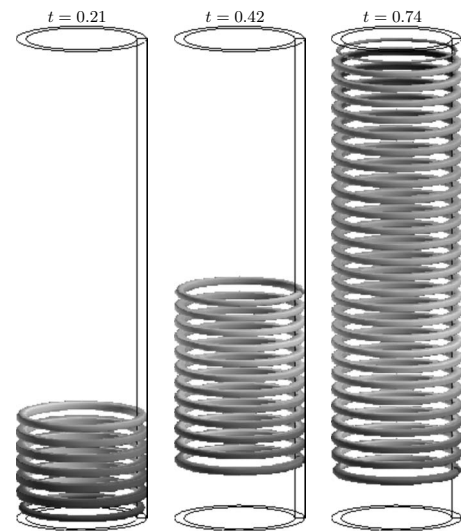


FIG. 12. Numerically obtained temporal evolution of the wave packet for  $Ta=215$ ,  $\alpha=-10$ , and  $\beta=10$ , exhibiting an absolute mode with  $n=0$ . Surfaces are fluctuations of axial velocity at slightly different levels.

$Ta=500-1100$ , well above  $Ta_{\text{crit}}^{\text{abs}}$  and corresponding to wavy, modulated wavy, and turbulent vortical flows.<sup>26</sup> The imaginary part  $\text{Im}(k_{\text{crit}})$  shown in Fig. 11(d) scales the steepness of the rising front, irrespective of the temporal growth. This steepness increases with  $\beta$  but saturates around  $\beta \approx 15$  with a characteristic length  $l=1/\text{Im}(k_{\text{crit}}) \approx 3$ . The phase velocity  $v_{\phi \text{ crit}}$  shown in Fig. 11(e) increases with  $\beta$  and negative  $\alpha$  for the  $n=0$  mode but remains low for  $n=-1$ . The phase velocity compared to the bulk axial velocity  $v_{\phi \text{ crit}}/\beta$  is shown in Fig. 11(f). While this ratio remains close to 1.2–1.3 for the helical mode, it strongly increases with  $\beta$  for the toroidal one, constituting another discrepancy with the convective instability.

The numerical simulation of the development and propagation of the vortical structure for an absolute axisymmetric mode corresponding to one of the dots in Fig. 10 ( $\alpha=-10$ ,  $\beta=10$ , and  $Ta=215$  to be compared to  $Ta_{\text{crit}}^{\text{abs}}=209.52$ ) is shown in Fig. 12. For these values of  $\alpha$  and  $\beta$ , both the convective and absolute most unstable modes are expected to be toroidal. Initially, the toroidal vortices appear at the upstream end of the annulus. As time progresses, the vortical structures spread further downstream, eventually filling the annulus. The spatiotemporal development of the vortical structures is shown in Fig. 13. Moreover, the temporal evolution of the kinetic energy associated with each azimuthal wave number  $|n|$  of the perturbation extracted from the numerical simulation, i.e., the sum over the three components of the velocity of the squared amplitudes of the Fourier coefficients in the azimuthal direction, is depicted in Fig. 14(a). The predominance of the  $n=0$  mode is obvious. The  $|n|=5$  mode is more than four orders of magnitude weaker than the predominant mode, confirming that the azimuthal resolution of the simulation is adequate. The vortical structure is made up of vortices of relatively uniform strength, unlike the wave packets of vortices for the convective instability, and it spreads axially more quickly than the average axial velocity of the base flow. The strength of the vortices is several orders

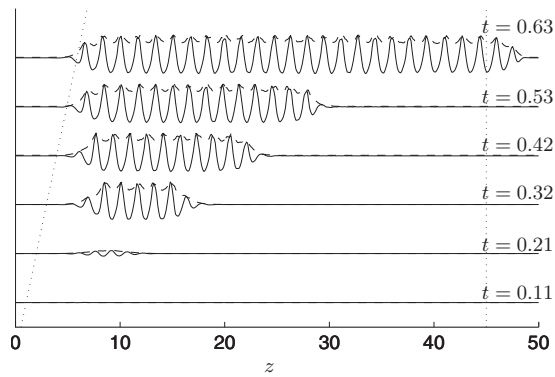


FIG. 13. Numerically obtained spatiotemporal evolution of the wave packet for  $Ta=215$ ,  $\alpha=-10$ , and  $\beta=10$  in the form of the axial velocity (—) and its spatial Hilbert transform (---) and, superposed, the point originally at  $z=0$  and traveling at the mean nondimensional axial velocity  $\beta=10$  (···). The buffer region used in the numerical simulation extends between  $z=45$  (···) and the outlet at  $z=50$ .

of magnitude greater than for the convective instability, and the sharp peaks and rounded troughs indicate nonlinearity in the structure. No vortices appear at the upstream end of the annulus due to the nonvortical flow imposed at the inlet. The flow clearly exhibits a front-forming pattern at constant finite length from the inlet. Without venturing further into the analysis of the nonlinear behavior of the flow, this shows strong similarities with the dynamics of the “healing length” of nonlinear global modes in semi-infinite domains, as addressed within the formalism of amplitude equations for cylindrical Couette flow with axial flow,<sup>61</sup> wakes,<sup>62</sup> and generic Ginzburg–Landau equations.<sup>63</sup> Vortices are intentionally damped out in the buffer region at the downstream end of the annulus.

The numerical simulation of the development and propagation of the vortical structure for an absolute axisymmetric mode corresponding to the other dot in Fig. 10 ( $\alpha=5$ ,  $\beta=15$ , and  $Ta=220$  to be compared to  $Ta_{crit}^{abs}=216.81$ ) is shown Fig. 15. Unlike the case of Fig. 12 where both the absolute and convective most unstable modes are axisymmetric, for these values of  $\alpha$  and  $\beta$ , the most convectively unstable mode is expected to be a single right-handed helix, although helices with  $n$  ranging from  $-6$  to  $9$  are expected to be convectively unstable. The initial instability is a double

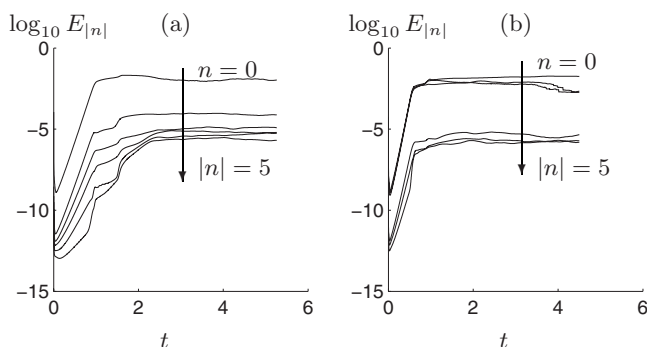


FIG. 14. Numerically obtained temporal evolution of the energies  $E_{|n|}$  associated with azimuthal modes  $n=0$  to  $|n|=5$  for (a)  $Ta=215$ ,  $\alpha=-10$ ,  $\beta=10$  and (b)  $Ta=220$ ,  $\alpha=5$ ,  $\beta=15$ .

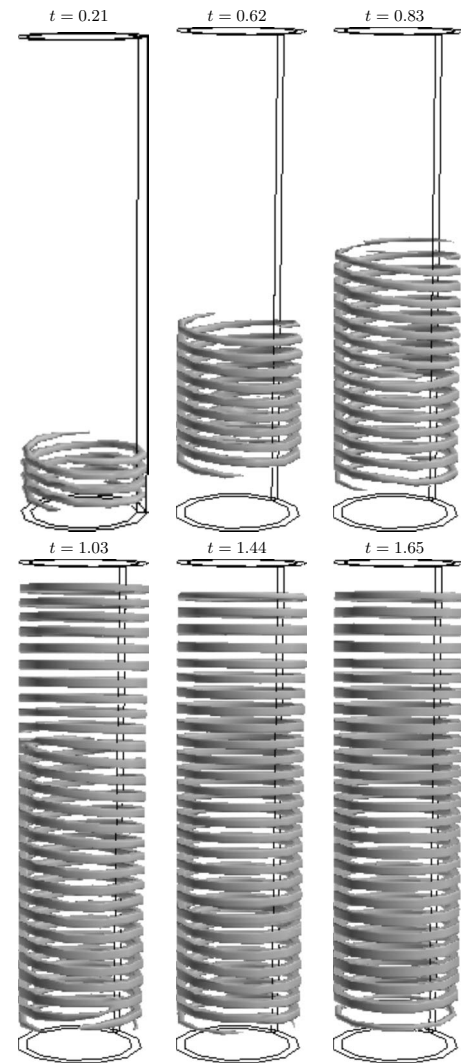


FIG. 15. Numerically obtained temporal evolution of the wave packet for  $Ta=220$ ,  $\alpha=5$ , and  $\beta=15$ , exhibiting an absolute mode with  $n=0$ . Surfaces are fluctuations of axial velocity at slightly different levels.

helical structure ( $t=0.21$ ). As the structure grows and propagates ( $t=0.62$ ), the trailing portion becomes a single helical structure, consistent with the  $n=1$  convective mode expected at these values for  $\alpha$  and  $\beta$ , while the leading portion remains a double helical structure ( $t=0.83$ ). Although helical structures persist near the inlet, the downstream portion fills in with axisymmetric vortices related to the absolute instability ( $t=1.03$ ). As time progresses, the axisymmetric absolute instability replaces the double helical structure, although the single helical structure remains near the inlet ( $t=1.44$ ). By the next time step shown, the entire annulus is filled with axisymmetric vortices of the absolute instability ( $t=1.65$ ). The spatiotemporal development of the structure, not shown here because the different structures cannot be discriminated in such a diagram, is similar to that shown in Fig. 13 with vortices of relatively uniform strength that spread axially more quickly than the average axial velocity of the base flow. The temporal evolution of the energy associated with each mode in the azimuthal direction is depicted in Fig. 14(b). Whereas the  $n=0$ ,  $|n|=1$ , and  $|n|=2$  modes are found to be of

comparable importance at initial times, the axisymmetric mode  $n=0$  eventually becomes predominant.

## V. CONCLUSIONS AND OUTLOOK

Owing to the conspicuous similarities between the body of experimental results and the computed convective instabilities, it is very likely that most of the experimental setups act as amplifiers of the noise at the inlet, fostering convective-type instabilities. The absolute modes are fairly elusive even in the numerical simulations as they tend to be overridden by convective instabilities triggered by the numerical noise. Similarly, the absolute modes are also expected to be difficult to observe experimentally. A way to alleviate this difficulty might be to use an experimental or numerical configuration where the gap of the annulus reduces at the inlet, inducing the *local* stability of the flow at the inlet by increasing  $\eta$  and  $\beta$ . Analytically, the framework of the stability analyses would then shift to global modes developing for the spatially varying (in the axial direction) base flow, as introduced in fluid mechanics in Refs. 47 and 64. These global modes are known to be driven by local absolute instability modes for configurations where the locally absolutely unstable region is of limited extent. These configurations have been extensively studied in the case of mixed Rayleigh–Bénard–Poiseuille convection.<sup>65,66</sup>

Of course, many discrepancies remain between the situation addressed in this study and experimental setups or filtration devices. These discrepancies pave the way for possible future work. First, one or two porous cylinders should be modeled to provide a more realistic boundary condition than the assumption of imposed wall-normal velocities. Second, the case of an inner porous cylinder and an outer non-porous cylinder could be considered. This, however, constitutes a significant challenge since there is no analytic solution for the base flow. Moreover, depending on the

relative pressure drops along the axial direction and across the porous cylinder, dramatic modifications of this base flow could result as the exhaustion of the axial flow or the reversal of the radial flow might occur. Furthermore, since fluid is lost through the inner cylinder, the axial flow decreases along the length of the annulus and vortices decrease in size. Again, the natural framework for the stability analysis of such a configuration amounts to global modes in semi-infinite domains this time. Finally, as hinted by the results of the numerical simulations, this system constitutes a worthwhile framework to analyze the nonlinear behavior of the convective/absolute and global modes of instability according to recent approaches.<sup>67</sup> However tantalizing, work along this line requires a large amount of analytical and numerical effort and is beyond the scope of the present paper, although it remains a longer term goal. Nevertheless, further insight into the problem gained by addressing these configurations could be applied to practical realizations such as rotating filtration.

## ACKNOWLEDGMENTS

The authors acknowledge the financial support of the Agence Nationale de la Recherche (ANR) (Program No. ANR-08-BLAN-0184-03) and the Centre National de la Recherche Scientifique/National Science Foundation (CNRS/NSF) joint program. The authors also acknowledge the Institut du Développement et des Ressources en Informatique Scientifique (IDRIS/CNRS, Orsay) computing center, where the computations were performed on a Nec SX8 supercomputer (Program No. 080242).

## APPENDIX: EXPRESSIONS FOR THE BASE FLOW

Starting from the incompressible Navier–Stokes equations, the laminar steady base flow is

$$\begin{cases} u_b = \frac{1 - \eta}{\eta} \frac{\alpha}{\text{Ta}} \frac{1}{r}, \\ v_b = \frac{r_{\text{in}}^2 r_{\text{out}}}{r_{\text{out}}^{\alpha+2} - r_{\text{in}}^{\alpha+2}} \left( \frac{r_{\text{out}}^{\alpha+1}}{r} - \frac{r^{\alpha+1}}{r_{\text{out}}} \right), \\ w_b = \frac{1 - \eta}{\eta} \frac{\beta}{\text{Ta}} (2 + \alpha) \frac{[r_{\text{out}}^2 (r_{\text{out}}^\alpha - r_{\text{in}}^\alpha) + r_{\text{in}}^2 (r_{\text{out}}^\alpha - r_{\text{in}}^\alpha) - r^2 (r_{\text{out}}^\alpha - r_{\text{in}}^\alpha)]}{(2 - \alpha)(r_{\text{out}}^{\alpha+2} - r_{\text{in}}^{\alpha+2}) + (2 + \alpha)(r_{\text{in}}^2 r_{\text{out}}^\alpha - r_{\text{out}}^2 r_{\text{in}}^\alpha)}, \end{cases} \quad (\text{A1})$$

provided  $\alpha \neq -2, 0, 2$ . For  $\alpha = -2$ , the base flow is

$$\begin{cases} u_b = -\frac{1 - \eta}{\eta} \frac{2}{\text{Ta}} \frac{1}{r}, \\ v_b = \frac{1}{\log(r_{\text{out}}/r_{\text{in}})} \frac{r_{\text{in}}^2 \log(r_{\text{out}}/r)}{r}, \\ w_b = \frac{1 - \eta}{\eta} \frac{\beta}{\text{Ta}} \frac{\frac{r^2 - r_{\text{out}}^2}{r_{\text{in}}^2} + \frac{r_{\text{in}}^2 - r^2}{r_{\text{out}}^2} + \frac{r_{\text{out}}^2 - r_{\text{in}}^2}{r^2}}{(r_{\text{in}}/r_{\text{out}})^2 - (r_{\text{out}}/r_{\text{in}})^2 + 4 \log(r_{\text{out}}/r_{\text{in}})}. \end{cases} \quad (\text{A2})$$

For  $\alpha = 0$ , the base flow is

$$\begin{cases} u_b = 0, \\ v_b = \frac{r_{in}^2 r_{out}}{r_{out}^2 - r_{in}^2} \left( \frac{r_{out}}{r} - \frac{r}{r_{out}} \right), \\ w_b = \frac{1 - \eta \beta}{\eta \text{Ta}} \frac{r_{out}^2 \log(r/r_{in}) + r_{in}^2 \log(r_{out}/r) - r^2 \log(r_{out}/r_{in})}{(r_{in}^2 + r_{out}^2) \log(r_{out}/r_{in}) - r_{out}^2 + r_{in}^2}. \end{cases} \quad (\text{A3})$$

And, finally, for  $\alpha=2$ , the base flow is

$$\begin{cases} u_b = \frac{1 - \eta \beta}{\eta \text{Ta}} \frac{1}{r}, \\ v_b = \frac{r_{in}^2 r_{out}}{r_{out}^4 - r_{in}^4} \left( \frac{r_{out}^3}{r} - \frac{r^3}{r_{out}} \right), \\ w_b = \frac{1 - \eta \beta}{\eta \text{Ta}} \frac{4}{r_{out}^2/r_{in}^2 - r_{in}^2/r_{out}^2 - 4} \frac{r_{out}^2/r_{in}^2 \log(r_{out}/r) + r^2/r_{out}^2 \log(r/r_{in}) - \log(r_{out}/r_{in})}{\log(r_{out}/r_{in})}. \end{cases} \quad (\text{A4})$$

The expression of the pressure field for the base flow is not included here since it is not required for the stability analysis.

- <sup>1</sup>G. Beaudoin and M. Y. Jaffrin, "Plasma filtration in Couette flow membrane devices," *Artif. Organs* **13**, 43 (1989).
- <sup>2</sup>R. M. Lueptow and A. Hajiloo, "Flow in a rotating membrane plasma separator," *Trans. Am. Soc. Artif. Intern. Organs* **41**, 182 (1995).
- <sup>3</sup>K. Ohashi, K. Tashiro, F. Kushiya, T. Matsumoto, S. Yoshida, M. Endo, T. Horio, K. Osawa, and K. Sakai, "Rotation-induced Taylor vortex enhances filtrate flux in plasma separation," *Trans. Am. Soc. Artif. Intern. Organs* **34**, 300 (1988).
- <sup>4</sup>G. Belfort, P. Mikulasek, J. M. Pimbley, and K. Y. Chung, "Diagnosis of membrane fouling using a rotating annular filter. 2. Dilute particulate suspension of known particle size," *J. Membr. Sci.* **77**, 23 (1993).
- <sup>5</sup>G. Belfort, J. M. Pimbley, A. Greiner, and K. Y. Chung, "Diagnosis of membrane fouling using a rotating annular filter. 1. Cell culture media," *J. Membr. Sci.* **77**, 1 (1993).
- <sup>6</sup>B. Hallström and M. Lopez-Leiva, "Description of a rotating ultrafiltration module," *Desalination* **24**, 273 (1978).
- <sup>7</sup>K. H. Kroner and V. Nissinen, "Dynamic filtration of microbial suspension using an axially rotating filter," *J. Membr. Sci.* **36**, 85 (1988).
- <sup>8</sup>A. Margaritis and C. R. Wilke, "The rotor fermentor. I. Description of the apparatus power requirements and mass transfer characteristics," *Biotechnol. Bioeng.* **20**, 709 (1978).
- <sup>9</sup>S. T. Wereley, A. Akonur, and R. M. Lueptow, "Particle-fluid velocities and fouling in rotating filtration of a suspension," *J. Membr. Sci.* **209**, 469 (2002).
- <sup>10</sup>J. A. Schwille, D. Mitra, and R. M. Lueptow, "Design parameters for rotating filtration," *J. Membr. Sci.* **204**, 53 (2002).
- <sup>11</sup>J. Kaye and E. C. Elgar, "Modes of adiabatic and diabatic fluid flow in an annulus with an inner rotating cylinder," *Trans. ASME* **80**, 753 (1958).
- <sup>12</sup>S. Chandrasekhar, "The hydrodynamic instability of viscous flow between coaxial cylinders," *Proc. Natl. Acad. Sci. U.S.A.* **46**, 141 (1960).
- <sup>13</sup>R. C. DiPrima, "The stability of a viscous fluid between rotating cylinders with an axial flow," *J. Fluid Mech.* **9**, 621 (1960).
- <sup>14</sup>R. J. Donnelly and D. Fultz, "Experiments on the stability of spiral flow between rotating cylinders," *Proc. Natl. Acad. Sci. U.S.A.* **46**, 1150 (1960).
- <sup>15</sup>K. W. Schwarz, B. E. Springlett, and R. J. Donnelly, "Modes of instability in spiral flow between rotating cylinders," *J. Fluid Mech.* **20**, 281 (1964).
- <sup>16</sup>K. C. Chung and K. N. Astill, "Hydrodynamic instability of viscous flow between rotating coaxial cylinders with fully developed axial flow," *J. Fluid Mech.* **81**, 641 (1977).
- <sup>17</sup>M. A. Haseon and B. W. Martin, "The stability of a viscous axial flow in an annulus with a rotating inner cylinder," *Proc. R. Soc. London, Ser. A* **352**, 351 (1977).

- <sup>18</sup>N. Gravas and B. W. Martin, "Instability of viscous axial flow in annuli having a rotating inner cylinder," *J. Fluid Mech.* **86**, 385 (1978).
- <sup>19</sup>B. S. Ng and E. R. Turner, "On the linear stability of spiral flow between rotating cylinders," *Proc. R. Soc. London, Ser. A* **382**, 83 (1982).
- <sup>20</sup>K. L. Babcock, G. Ahlers, and D. S. Cannell, "Noise-sustained structure in Taylor–Couette flow with through-flow," *Phys. Rev. Lett.* **67**, 3388 (1991).
- <sup>21</sup>A. Recktenwald, M. Lücke, and H. W. Müller, "Taylor vortex formation in axial through-flow: Linear and weakly nonlinear analysis," *Phys. Rev. E* **48**, 4444 (1993).
- <sup>22</sup>E. C. Johnson and R. M. Lueptow, "Hydrodynamic stability of flow between rotating porous cylinders with radial and axial flow," *Phys. Fluids* **9**, 3687 (1997).
- <sup>23</sup>H. A. Snyder, "Experiments on the stability of spiral flow at low axial Reynolds numbers," *Proc. R. Soc. London, Ser. A* **265**, 198 (1962).
- <sup>24</sup>M. M. Sorour and J. E. R. Coney, "The characteristics of spiral vortex flow at high Taylor numbers," *J. Mech. Eng. Sci.* **21**, 65 (1979).
- <sup>25</sup>R. C. DiPrima and A. Pridor, "The stability of viscous flow between rotating concentric cylinders with an axial flow," *Proc. R. Soc. London, Ser. A* **366**, 555 (1979).
- <sup>26</sup>R. M. Lueptow, A. Docter, and K. Min, "Stability of axial flow in an annulus with a rotating inner cylinder," *Phys. Fluids A* **4**, 2446 (1992).
- <sup>27</sup>D. I. Takeuchi and D. F. Jankowski, "A numerical and experimental investigation of the stability of spiral Poiseuille flow," *J. Fluid Mech.* **102**, 101 (1981).
- <sup>28</sup>S. T. Wereley and R. M. Lueptow, "Velocity field for Taylor–Couette flow with an axial flow," *Phys. Fluids* **11**, 3637 (1999).
- <sup>29</sup>K. Bühler, "Instabilitäten spiralförmiger Strömungen im Zylinderspalt," *Z. Angew. Math. Mech.* **64**, 180 (1984).
- <sup>30</sup>K. Bühler, "Symmetric and asymmetric Taylor vortex flow in spherical gaps," *Acta Mech.* **81**, 3 (1990).
- <sup>31</sup>K. Min and R. M. Lueptow, "Circular Couette flow with pressure-driven axial flow and a porous inner cylinder," *Exp. Fluids* **17**, 190 (1994).
- <sup>32</sup>A. Kolyshkin and R. Vaillancourt, "Convective instability boundary of Couette flow between rotating porous cylinder with axial and radial flow," *Phys. Fluids* **9**, 910 (1997).
- <sup>33</sup>A. Meseguer and F. Marques, "On the competition between centrifugal and shear instability in spiral Poiseuille flow," *J. Fluid Mech.* **455**, 129 (2002).
- <sup>34</sup>D. L. Cotrell and A. J. Pearlstein, "The connection between centrifugal instability and Tollmien–Schlichting-like instability for spiral Poiseuille flow," *J. Fluid Mech.* **509**, 331 (2004).
- <sup>35</sup>D. L. Cotrell, S. L. Rani, and A. J. Pearlstein, "Computational assessment of subcritical and delayed onset in spiral Poiseuille flow experiments," *J. Fluid Mech.* **509**, 353 (2004).
- <sup>36</sup>A. Meseguer and F. Marques, "On the stability of medium gap corotating spiral Poiseuille flow," *Phys. Fluids* **17**, 094104 (2005).
- <sup>37</sup>C. J. Heaton, "Optimal linear growth in spiral Poiseuille flow," *J. Fluid Mech.* **607**, 141 (2008).

- <sup>38</sup>S. K. Bahl, "Stability of viscous flow between two concentric rotating porous cylinders," *Def. Sci. J.* **20**, 89 (1970).
- <sup>39</sup>K. Bühler, in *Ordered and Turbulent Patterns in Taylor–Couette Flow*, edited by E. D. Andereck and F. Hayot (Plenum, New York, 1992), pp. 197–203.
- <sup>40</sup>T. S. Chang and W. K. Sartory, "Hydromagnetic stability of dissipative flow between rotating permeable cylinders," *J. Fluid Mech.* **27**, 65 (1967).
- <sup>41</sup>T. S. Chang and W. K. Sartory, "Hydromagnetic stability of dissipative flow between rotating permeable cylinders. Part 2. Oscillatory critical modes and asymptotic results," *J. Fluid Mech.* **36**, 193 (1969).
- <sup>42</sup>K. Min and R. M. Lueptow, "Hydrodynamic stability of viscous flow between rotating porous cylinders with radial flow," *Phys. Fluids* **6**, 144 (1994).
- <sup>43</sup>E. Serre, M. A. Sprague, and R. M. Lueptow, "Stability of Taylor–Couette flow in a finite-length cavity with radial through-flow," *Phys. Fluids* **20**, 034106 (2008).
- <sup>44</sup>S. Lee and R. M. Lueptow, "Rotating membrane filtration and rotating reverse osmosis," *J. Chem. Eng. Jpn.* **37**, 471 (2004).
- <sup>45</sup>S. K. Bahl and K. M. Kapur, "The stability of a viscous flow between two concentric rotating porous cylinders with an axial flow," *Def. Sci. J.* **25**, 139 (1975).
- <sup>46</sup>P. Huerre and P. A. Monkewitz, "Absolute and convective instabilities in free shear layers," *J. Fluid Mech.* **159**, 151 (1985).
- <sup>47</sup>P. Huerre and P. A. Monkewitz, "Local and global instabilities in spatially developing flows," *Annu. Rev. Fluid Mech.* **22**, 473 (1990).
- <sup>48</sup>A. Tsameret, G. Goldner, and V. Steinberg, "Experimental evaluation of the intrinsic noise in the Couette–Taylor system with an axial flow," *Phys. Rev. E* **49**, 1309 (1994).
- <sup>49</sup>A. Tsameret and V. Steinberg, "Noise-modulated propagating pattern in a convectively unstable system," *Phys. Rev. Lett.* **67**, 3392 (1991).
- <sup>50</sup>F. Marques, J. Sanchez, and P. D. Weidman, "Generalized Couette–Poiseuille flow with boundary mass transfer," *J. Fluid Mech.* **374**, 221 (1998).
- <sup>51</sup>O. Czarny and R. M. Lueptow, "Time scales for transition in Taylor–Couette flow," *Phys. Fluids* **19**, 054103 (2007).
- <sup>52</sup>O. Czarny, E. Serre, P. Bontoux, and R. M. Lueptow, "Spiral and wavy vortex flows in short counter-rotating Taylor–Couette cells," *Theor. Comput. Fluid Dyn.* **16**, 5 (2002).
- <sup>53</sup>O. Czarny, E. Serre, P. Bontoux, and R. M. Lueptow, "Interaction between Ekman pumping and the centrifugal instability in Taylor–Couette flow," *Phys. Fluids* **15**, 467 (2003).
- <sup>54</sup>O. Czarny, E. Serre, P. Bontoux, and R. M. Lueptow, "Ekman vortices and the centrifugal instability in counter-rotating cylindrical Couette flow," *Theor. Comput. Fluid Dyn.* **18**, 151 (2004).
- <sup>55</sup>E. Serre, E. C. del Arco, and P. Bontoux, "Annular and spiral patterns in flows between rotating and stationary discs," *J. Fluid Mech.* **434**, 65 (2001).
- <sup>56</sup>J. M. Vanel, R. Peyret, and P. Bontoux, in *Numerical Methods for Fluid Dynamics II*, edited by K. W. Morton and M. J. Baines (Clarendon, Oxford, 1986), pp. 463–475.
- <sup>57</sup>I. Raspo, S. Hughes, E. Serre, A. Randriamampianina, and P. Bontoux, "A spectral projection method for the simulation of complex three-dimensional rotating flows," *Comput. Fluids* **31**, 745 (2002).
- <sup>58</sup>V. Sobolik, B. Izrar, F. Lusseyran, and S. Skali, "Interaction between the Ekman layer and the Couette–Taylor instability," *Int. J. Heat Mass Transfer* **43**, 4381 (2000).
- <sup>59</sup>H. A. Snyder, "Experiments on the stability of two types of spiral flow," *Ann. Phys.* **31**, 292 (1965).
- <sup>60</sup>S. Leibovich and K. Stewartson, "A sufficient condition for the instability of columnar vortices," *J. Fluid Mech.* **126**, 335 (1983).
- <sup>61</sup>P. Büchel, M. Lücke, D. Roth, and R. Schmitz, "Pattern selection in the absolutely unstable regime as a nonlinear eigenvalue problem: Taylor vortices in axial flow," *Phys. Rev. E* **53**, 4764 (1996).
- <sup>62</sup>I. Delbende and J.-M. Chomaz, "Nonlinear convective/absolute instabilities in parallel two-dimensional wakes," *Phys. Fluids* **10**, 2724 (1998).
- <sup>63</sup>A. Couairon and J.-M. Chomaz, "Absolute and convective instabilities, front velocities, and global modes in nonlinear systems," *Physica D* **108**, 236 (1997).
- <sup>64</sup>P. A. Monkewitz, P. Huerre, and J.-M. Chomaz, "Global linear stability analysis of weakly nonparallel shear flows," *J. Fluid Mech.* **288**, 1 (1993).
- <sup>65</sup>P. Carrière and P. A. Monkewitz, "Transverse-roll global modes in a Rayleigh–Bénard–Poiseuille convection," *Eur. J. Mech. B/Fluids* **20**, 751 (2001).
- <sup>66</sup>D. Martinand, P. Carrière, and P. A. Monkewitz, "Three-dimensional global instability modes associated with a localized hot spot in Rayleigh–Bénard–Poiseuille convection," *J. Fluid Mech.* **551**, 275 (2006).
- <sup>67</sup>J.-M. Chomaz, "Global instabilities in spatially developing flows: Non-normality and nonlinearity," *Annu. Rev. Fluid Mech.* **37**, 357 (2005).